Clutter Suppression Approach for End-Fire Array Airborne Radar Based on Adaptive Segmentation

YONGWEI LI, **WENCHONG XIE**, **(Member, IEEE)**, **HUIHUANG MAO**, **AND RUIJIE DONG**
Wuhan Early Warning Academy, Wuhan 430019, China
Corresponding author: Wenchong Xie (xwch1978@163.com)

ABSTRACT End-fire array antenna is a kind of special radar antenna with beam pointing perpendicular to the normal direction of the array. Because of its low profile and directional radiation characteristics, it is especially suitable for blind zone compensation of airborne radar. However, there are few publicly available pieces of literature on clutter suppression for end-fire array radar. In this paper, we firstly simulate and analyze the clutter spectrum characteristics for end-fire array airborne radar (EAAR), and then propose a clutter suppression method for EAAR based on adaptive segmentation. In the proposed method, the concept of Riemann mean distance of temporal covariance matrix is introduced to quantify the clutter nonstationarity, and in this way we realize adaptive segmentation of the clutter range-Doppler spectrum. Then the different clutter suppression methods including pulse Doppler (PD) processing, two-dimensional space-time adaptive processing (2D STAP), and three-dimensional STAP (3D STAP) are used to suppress clutter in different regions. The theoretical analysis and simulation results demonstrate that compared with 3D STAP, the proposed method not only guarantees clutter suppression performance, but also reduces the computational complexity to an extent.

INDEX TERMS End-fire array, clutter suppression, adaptive segmentation, Riemann mean distance.

I. INTRODUCTION

With the rapid development of conformal and quasi-conformal array radar [1]–[4], end-fire array antenna [5]–[9] has attracted wide attention in recent years due to its unique low profile characteristics. Because the maximum radiation direction of end-fire array antenna points to the array arrangement axis, its directional coefficient in the maximum radiation direction is no longer directly proportional to the equivalent aperture size, which effectively solves the problem of larger wind resistance caused by larger aperture size of the side-fire array. Hence, end-fire array antenna is especially suitable for forward and backward blind zone compensation of airborne radar. However, the primary problem must be solved in the practical engineering application of end-fire array airborne radar (EAAR) is clutter suppression. To solve this problem, we must study its clutter spectrum characteristics and propose effective space-time adaptive processing (STAP) methods. At present, the research on end-fire array in existing literature mainly focuses on antenna characteristics [5]–[9], and almost no literature involves clutter suppression for EAAR. Although some countries have had

relatively mature technology in the application of end-fire array radar and have put it into practice, such as the 'E-737' early warning aircraft developed by the United States, which uses end-fire array antenna for blind zone compensation forward and backward. However, considering technical confidentiality, the relevant literature concerning the research on clutter and STAP methods for EAAR is still not available.

In this paper, we firstly construct the geometric model of EAAR with uniform linear array as the end-fire unit. On the basis of that, the antenna pattern characteristics and the clutter spectrum characteristics of EAAR are simulated and analyzed. By comparing these with that of conventional side-fire array airborne radar (SAAR), a series of useful conclusions are obtained. In the basis of this, we proposed a novel clutter suppression method for EAAR based on adaptive segmentation. In the proposed method, we introduce the concept of Riemann mean distance to quantify the clutter nonstationarity and divide the clutter range-Doppler spectrum into three sections including pure noise region, stationary clutter region, and nonstationary clutter region by adaptive segmentation. Then the different clutter suppression methods including pulse Doppler (PD) processing, two-dimensional space-time adaptive processing (2D STAP) [10]–[12], and three-dimensional STAP (3D STAP) [13], [14] are used to

---

The associate editor coordinating the review of this manuscript and approving it for publication was Giorgio Montisci.

suppress clutter in corresponding sections. Simulation results illustrate the effectiveness of the proposed method.

The rest of this paper is organized as follows. Section 2 simulates the clutter and analyzes the clutter characteristics for EAAR. Section 3 introduces the proposed method based on adaptive segmentation. Performance of this method is illustrated by computer simulations and conclusions are drawn in Sections 5 and 6, respectively.

Notations: Scalars are denoted by lightfaced lowercase letters, vectors by boldfaced lowercase letters, and matrices by boldfaced uppercase letters. $(\cdot)^{\mathrm{T}}$ denotes transpose, the superscript $(\cdot)^{\mathrm{H}}$ denotes conjugate transpose, $(\cdot)^{-1}$ is the matrix inverse operation. $\otimes$ denotes the Kronecker product, denotes rounding down, $\|\cdot\|_{\mathrm{F}}$ denotes Frobenius norm. $\mathrm{E}[\cdot]$ denotes the statistical expectation. I denotes an identity matrix.

II. CLUTTER CHARACTERISTICS FOR EAAR
A. PATTERN CHARACTERISTICS

Consider an EAAR with a rectangular planar end-fire array antenna consisting of $M \times N$ elements, as shown in Fig. 1 (a). The column-subarrays are the end-fire units. The platform is at altitude H and moving with constant velocity V. The normal of the array is perpendicular to the flight direction of the platform, and the column-subarrays are parallel to the flight direction. The spacings between columns and rows are d_{x} and d_{y}, respectively. The working wavelength is λ. The angles θ and φ denote the azimuth and elevation angle, respectively. Moreover, (θ_0, φ_0) denotes the direction of the mainbeam and R denotes the range from the clutter scatter to the radar antenna. For ease of comparison, Fig. 1 (b) gives the array geometric model for SAAR.

According to the geometry in Fig. 1, the transmit pattern function of end-fire column-subarrays can be obtained as

$$f_1(\theta, \varphi) = \sum_{m=1}^{M} \exp\left\{ j\frac{2\pi d_{\mathrm{y}}}{\lambda}(m-1)(\cos\varphi\sin\theta - 1) \right\} \quad (1)$$

where the beam pointing is fixed to be $(0°, 90°)$ for the column-subarrays are end-fire units. And that of end-fire row-subarrays can be obtained as

$$\begin{aligned} f_2(\theta, \varphi) \\ = \sum_{n=1}^{N} \exp\left\{ j\frac{2\pi d_{\mathrm{x}}}{\lambda}(n-1)(\cos\varphi\cos\theta - \cos\varphi_0\cos\theta_0) \right\} \end{aligned} \quad (2)$$

Then the transmit pattern function of the whole end-fire array antenna can be expressed as

$$\begin{aligned} F_{\mathrm{e}}(\theta, \varphi) = \sum_{n=1}^{N}\sum_{m=1}^{M} \exp\left\{ j\frac{2\pi}{\lambda}\left[(m-1)d_{\mathrm{y}}(\cos\varphi\sin\theta - 1) \right.\right. \\ \left.\left. + (n-1)d_{\mathrm{x}}(\cos\varphi\cos\theta - \cos\varphi_0\cos\theta_0) \right] \right\} \end{aligned} \quad (3)$$
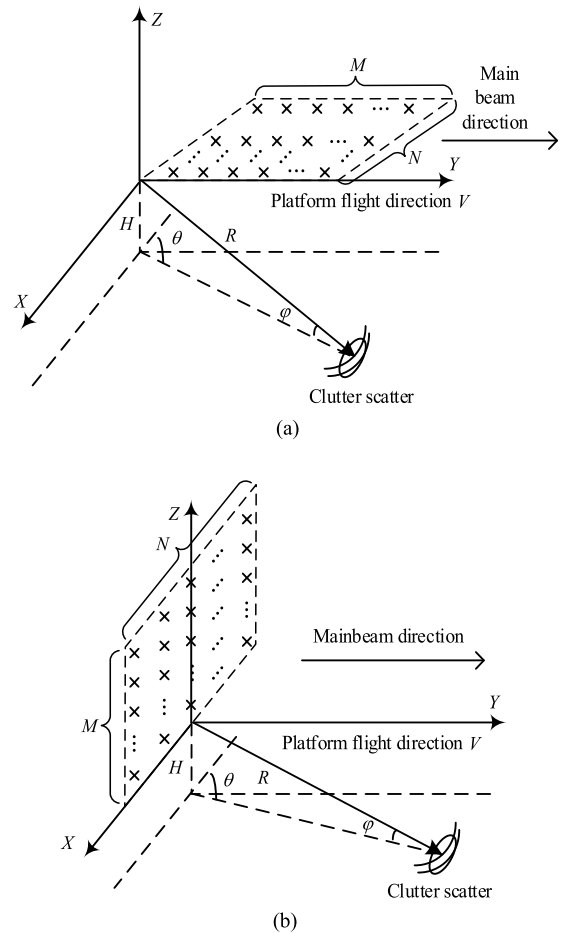

FIGURE 1. Array geometric model. (a) EAAR. (b) SAAR.

Whereas for side-fire array antenna, the transmit pattern function is

$$\begin{aligned} F_{\mathrm{e}}(\theta, \varphi) = \sum_{n=1}^{N}\sum_{m=1}^{M} \exp\left\{ j\frac{2\pi}{\lambda}\left[(m-1)d_{\mathrm{y}}(\sin\varphi - \sin\varphi_0) \right.\right. \\ \left.\left. + (n-1)d_{\mathrm{x}}(\cos\varphi\cos\theta - \cos\varphi_0\cos\theta_0) \right] \right\} \end{aligned} \quad (4)$$

Fig.2 (a) demonstrates the transmit pattern of EAAR with $M = 32$, $N = 16$, the main beam-pointing $(\theta_0, \varphi_0) = (90°, 0°)$, and $d_{\mathrm{x}} = \lambda/2$. Since end-fire array is placed horizontally and has no backward shielding reflection, we let d_{y} be equal to $\lambda/4$ to eliminate the backward grating lobe. Whereas Fig. 2 (b) shows the antenna transmit pattern of SAAR with 16 rows and 32 columns, $d_{\mathrm{x}} = d_{\mathrm{y}} = \lambda/2$. Other parameters are the same as EAAR.

Comparing Fig. 2 (a) with Fig. 2 (b), we can obtain that the antenna pattern of EAAR has the following characteristics.

(1) The SAAR has only one mainlobe because of the shielding effect of the reflector, whereas the EAAR has no backward shielding due to the horizontal array. Although the backward grating lobes are eliminated
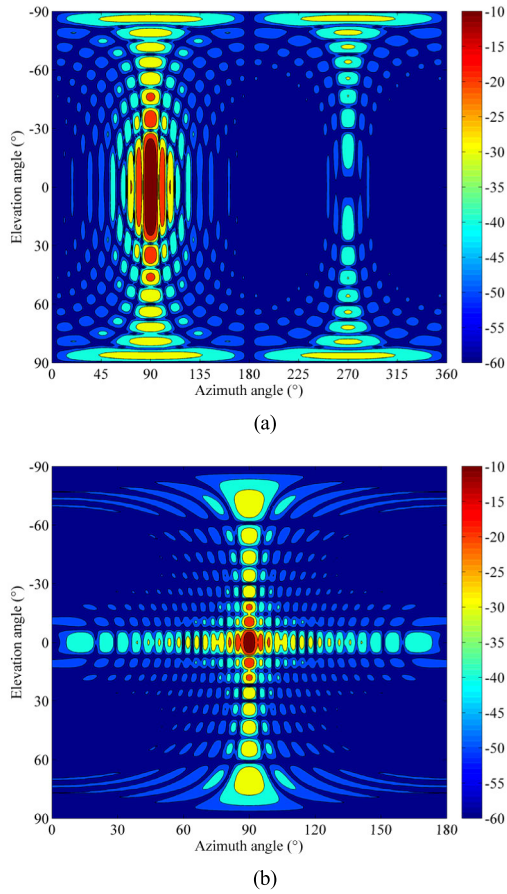
(a)

(b)

FIGURE 2. Antenna transmit patterns. (a) EAAR. (b) SAAR.

by reducing the inter-column spacing, the backward elevation sidelobes still exist.

(2) The mainlobe elevation beam width of EAAR is much wider than that of SAAR.

(3) The antenna pattern sidelobes of SAAR are distributed along the azimuth and elevation directions respectively in the form of "+" whereas that of EAAR are concentrated along the elevation direction in the form of "|". The apparent beams broadening in azimuth when the elevation angle is large is an illusion caused by the selection of coordinate system.

B. CLUTTER CHARACTERISTICS

Assuming that K pulses are transmitted at a constant pulse repetition frequency (PRF) in a coherent processing interval (CPI), the receive space-time sampled clutter echo signal on a range ring can be expressed as

$$X_c = \sum_{i_a=1}^{N_a} \sum_{i=1}^{N_c} A(\theta_i, \varphi_{i_a}) S(\theta_i, \varphi_{i_a}) \quad (5)$$

where $A(\theta_i, \varphi_{i_a})$ is the clutter amplitude at the clutter patch $(\theta_i, \varphi_{i_a})$, N_a is the number of range ambiguities, N_c is the number of clutter patches contained in a range ring, and $S(\theta_i, \varphi_{i_a})$ is the space time steering vector of clutter echoes.

If only two dimensions are considered, for both EAAR and SAAR, the steering vector $S(\theta_i, \varphi_{i_a})$ can be written as

$$S(\theta_i, \varphi_{i_a}) = S_A(\theta_i, \varphi_{i_a}) \otimes S_T(\theta_i, \varphi_{i_a}) \quad (6)$$

Adding elevation dimension information, then

$$S(\theta_i, \varphi_{i_a}) = S_E(\theta_i, \varphi_{i_a}) \otimes S_A(\theta_i, \varphi_{i_a}) \otimes S_T(\theta_i, \varphi_{i_a}) \quad (7)$$

The specific formulas of the three steering vectors are

$$S_E(\theta_i, \varphi_{i_a}) = \begin{bmatrix} 1 & e^{j2\pi f_e(\theta_i, \varphi_{i_a})} & \dots & e^{j2\pi(M-1)f_e(\theta_i, \varphi_{i_a})} \end{bmatrix}^T \quad (8)$$

$$S_A(\theta_i, \varphi_{i_a}) = \begin{bmatrix} 1 & e^{j2\pi f_a(\theta_i, \varphi_{i_a})} & \dots & e^{j2\pi(N-1)f_a(\theta_i, \varphi_{i_a})} \end{bmatrix}^T \quad (9)$$

$$S_T(\theta_i, \varphi_{i_a}) = \begin{bmatrix} 1 & e^{j2\pi f_t(\theta_i, \varphi_{i_a})} & \dots & e^{j2\pi(K-1)f_t(\theta_i, \varphi_{i_a})} \end{bmatrix}^T \quad (10)$$

where $f_e(\theta_i, \varphi_{i_a})$ is the normalized elevation spatial frequency, $f_a(\theta_i, \varphi_{i_a})$ is the normalized azimuth spatial frequency, and $f_t(\theta_i, \varphi_{i_a})$ is the normalized Doppler frequency. For side-fire forward looking array

$$f_a(\theta_i, \varphi_{i_a}) = (d_y/\lambda) \cos\theta_i \cos\varphi_{i_a} \quad (11)$$
$$f_e(\theta_i, \varphi_{i_a}) = (d_x/\lambda) \sin\varphi_{i_a} \quad (12)$$

Whereas for end-fire array

$$f_a(\theta_i, \varphi_{i_a}) = (d_x/\lambda) \cos\theta_i \cos\varphi_{i_a} \quad (13)$$
$$f_e(\theta_i, \varphi_{i_a}) = (d_y/\lambda) \sin\theta_i \cos\varphi_{i_a} \quad (14)$$

Since both SAAR and EAAR are forward-looking, the normalized Doppler frequencies of them are

$$f_t(\theta_i, \varphi_{i_a}) = 2V \sin\theta_i \cos\varphi_{i_a}/(f_r\lambda) \quad (15)$$

where f_r denotes the PRF.

In order to clarify the space time coupling relationship in the three-dimensional clutter spectrum for SAAR, combining (11), (12), and (15) yields

$$\frac{f_e^2(\theta_i, \varphi_{i_a})}{f_{em}^2} + \frac{f_a^2(\theta_i, \varphi_{i_a})}{f_{am}^2} + \frac{f_t^2(\theta_i, \varphi_{i_a})}{f_{tm}^2} = 1 \quad (16)$$

Whereas for EAAR, combining (13), (14), and (15) yields

$$\begin{cases} \dfrac{f_e(\theta_i, \varphi_{i_a})}{f_{em}} = \dfrac{f_t(\theta_i, \varphi_{i_a})}{f_{tm}} \\ \dfrac{f_a^2(\theta_i, \varphi_{i_a})}{f_{am}^2} + \dfrac{f_t^2(\theta_i, \varphi_{i_a})}{f_{tm}^2} = \cos^2\varphi_{i_a} \end{cases} \quad (17)$$

where f_{em} is the maximum normalized elevation spatial frequency, f_{am} is the maximum normalized azimuth spatial frequency, and f_{tm} is the maximum normalized Doppler frequency.

Formulas (16) and (17) show that in three dimensional clutter spectrum of SAAR, the three dimensions are ellipsoidal coupling, whereas in that of EAAR, the spatial elevation dimension is linear coupling with the temporal Doppler

dimension and the spatial azimuth dimension is elliptical nonlinear coupling with the temporal Doppler dimension.

In order to further analyze the clutter characteristics, we simulate the clutter spectrum of EAAR and SAAR. According to the engineering application examples, we assume that end-fire array is 16 rows and 8 columns, and side-fire array is 16 columns and 8 rows. The receive antenna pattern is tapered by 20 dB Chebyshev window. The other simulation parameters are listed in Table 1.

TABLE 1. Simulation parameters.

Parameter	Value
Mainbeam azimuth	90 degree
Mainbeam elevation	0 degree
Pulse number in one CPI	8
Spacing between columns	0.115m
Spacing between rows	0.058m
Working wavelength	0.23m
Platform moving velocity	140m/s
Pulse repetition frequency	2435Hz
Platform height	8km
Maximum detectable range	368km
Range cell width	100m

Fig. 3 shows the three-dimensional clutter ridges of SAAR and EAAR and their projections in azimuth-Doppler plane, i.e., conventional two-dimensional clutter ridge, respectively. In Fig. 3, we can see that the three-dimensional clutter ridges of SAAR are distributed along a quarter ellipsoid, and the clutter ridge in the same range have the same elevation spatial frequency. Therefore, it is feasible to form a notch in elevation dimension to filter the short-range nonstationary clutter. Whereas for EAAR, the three-dimensional clutter ridges are all distributed on a certain plane and the elevation spatial frequencies of the clutter ridge in the same range are different. Hence, the elevation-dimensional pre-filtering methods [15]–[17] which filter out short-range nonstationary clutter by forming an adaptive elevation notch will completely fail for EAAR. Meanwhile, the conventional two-dimensional, i.e., azimuth-Doppler dimension, clutter ridges of the two systems are elliptical and have serious range dependence in short range, but the long-range clutter tends to be stationary. Therefore, the conventional 2D STAP is still applicable to the long-range stationary clutter of EAAR.

Fig. 4 depicts the clutter range-Doppler spectrum of ideal echo data in a receive channel of SAAR and EAAR, respectively. It can be seen from Fig. 4 that the distinctions between SAAR and EAAR in antenna patterns analyzed above leads to the scattering of sidelobe clutter and the wider frequency domain of ground clutter for SAAR. Compared with SAAR,
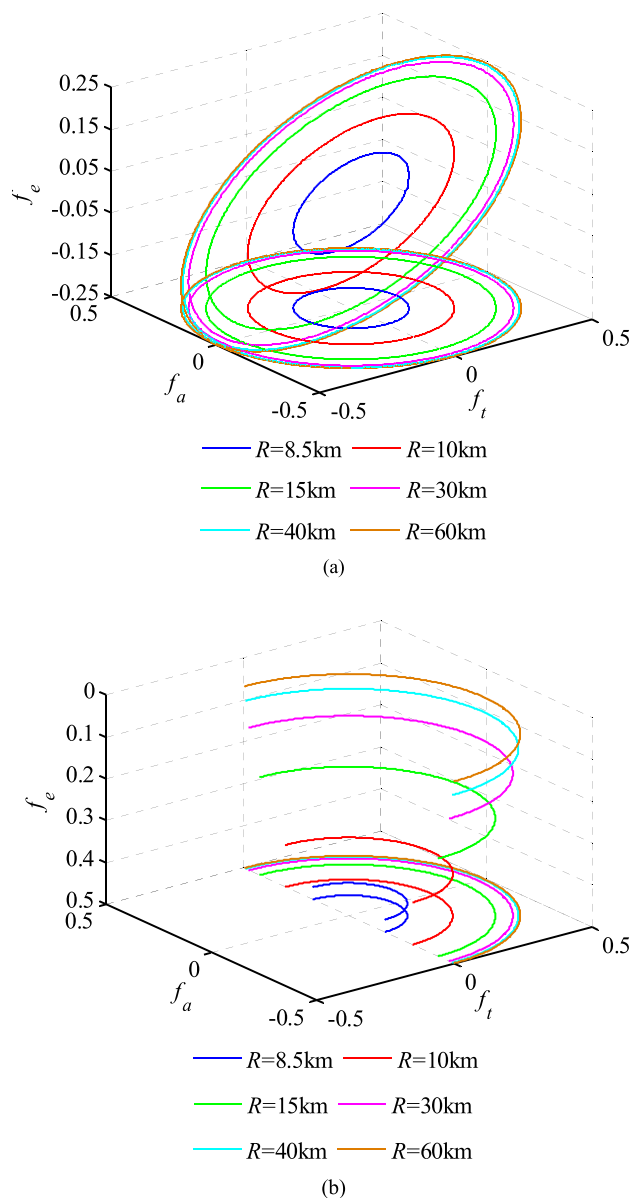

(a)

(b)

FIGURE 3. Three-dimensional clutter ridges. (a) EAAR. (b) SAAR.

clutter of EAAR is concentrated in the mainlobe region, and it occupies a narrower frequency domain, especially in the long-range stationary clutter region, i.e., there is a wider pure noise region in the long-range. Therefore, PD processing technique can be considered to detect moving targets in the long-range noise region for EAAR.

III. STAP BASED ON ADAPTIVE SEGMENTATION

Through the analysis in Section II, it can be seen that end-fire array antenna is usually placed forward-looking, so it also inevitably faces the problem of clutter range dependence. Although the conventional STAP approaches exhibit excellent performance on suppressing stationary clutter, the range-dependent clutter will lead to its failure to form deep and
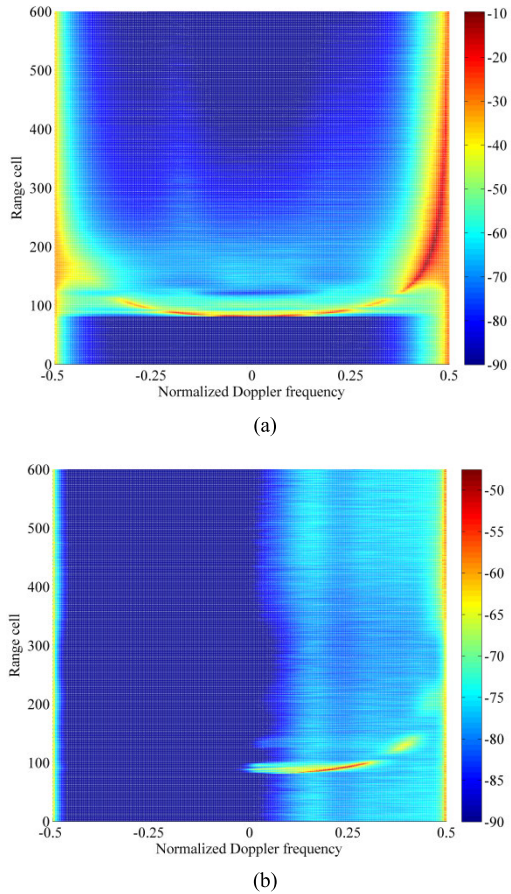
(a)

(b)

FIGURE 4. Clutter range-Doppler spectrum. (a) EAAR, (b) SAAR.

narrow filter notches, which will cause serious performance degradation and make it impossible to detect moving targets.

To solve the problem of clutter range dependence of SAAR, scholars have done a lot of research. At present, the nonstationary clutter suppression methods with range ambiguity mainly include improved registration-based compensation (RBC) method [18], elevation-dimensional pre-filtering STAP and 3D STAP. The improved RBC method takes full account of ambiguous clutter data on different clutter ridges of the same range cell, and has good range-dependent compensation effect when range ambiguity exists. However, in the process of clutter compensation, the improved RBC method will also cause the moving or cancellation of the target echo. Although it can effectively suppress clutter, it is not conducive to the subsequent target detection, it is also a common problem in all clutter-compensation methods when range ambiguity exists. Reference [19] studies the problem of moving or cancellation of the target echo while compensating clutter. It is proposed that the target constraint matrix can be used to restrain the target echoes from moving or cancellation. However, it is almost unachievable for the target constraint point to avoid all the clutter echoes in practical application, clutter will probably be wrongly retained as targets and result in false alarm. The

elevation-dimensional pre-filtering STAP takes advantage of the distinctions in elevation angle between the short-range clutter and the long-range clutter, form a notch in the elevation dimension to filter out the short-range nonstationary clutter fundamentally, and then suppress the long-range clutter by the conventional STAP method. It can be applied to the situation of existing range ambiguity without target echoes cancellation. However, the analysis in Section 2 shows that due to the special array arrangement structure of end-fire array antenna, the elevation spatial steering vector is not only related to the elevation angle, but also to the azimuth angle, so it is not feasible to utilize the elevation spatial steering vector to form a single elevation filter notch. 3D STAP is the generalization of the conventional azimuth-Doppler 2D STAP in azimuth-elevation-Doppler three dimensions. The simulation results in [13] demonstrate that 3D STAP can significantly improve the nonstationary clutter suppression performance by adding the degree of freedom (DOF) of elevation dimension. Hence, at present, only the 3D STAP can effectively solve the nonstationary clutter problem of EAAR. But 3D STAP also has the drawback that it has trouble to implement real-time processing because of the large sample demands and complex calculation.

Based on the analysis of clutter characteristics for EAAR in Section II, this section proposes a clutter suppression method based on adaptive segmentation. Compared with 3D STAP, this method reduces the computation load and sample demands significantly whereas the performance loss is small. Compared with 2D STAP, this method can effectively suppress the nonstationary clutter and ensure the effective detection of the target.

As depicted in Fig. 5, according to the difference of clutter intensity or nonstationary degree in the range-Doppler spectrum, the whole range-Doppler spectrum can be divided into three sections: nonstationary clutter region, stationary clutter region and noise region. And then, 3D STAP, conventional 2D STAP and PD processing method are applied to the corresponding sections. Therefore, the emphasis and difficulty of the proposed method are how to realize adaptive segmentation. The specific implementation process is as follows.
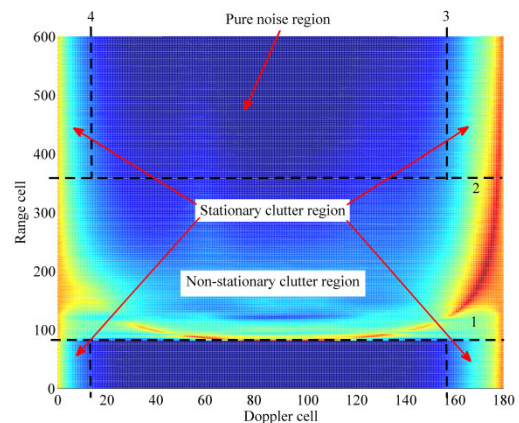

FIGURE 5. Regions dividing diagram.

A. ADAPTIVE SEGMENTATION OF NONSTATIONARY CLUTTER REGION

As can be seen from Fig. 1 (a), the nearest ground clutter to the radar antenna is the altitude-line clutter directly below the platform, i.e., the short range clutter at $R = H$. Therefore, the range cell corresponding to the altitude-line clutter is the initial range cell in the nonstationary clutter region, and its range cell number can be calculated by

$$L_l = \text{int}(H/\Delta R) \qquad (18)$$

where ΔR denotes the range cell width. So according to the parameters listed in Table 1, the 80th range cell can be easily calculated as the dividing line 1. Therefore, the emphasis of this section is how to realize the adaptive selection of dividing line 2. We can obtain from Fig. 4 that the essence of clutter nonstationarity is clutter power distribution in Doppler domain varies with range. Because the temporal clutter covariance matrix just contains the clutter power distribution information in Doppler domain, we can consider using the distinction between temporal covariance matrices in different range cells to measure the clutter nonstationarity.

For pulse Doppler radar, clutter signal of a range cell can be modeled as the superposition of clutter echoes in the range ring on the pulse dimension. For the nth element, supposing the clutter data of the lth range cell received by K pulses is $X_l((n-1)K+1:nK)$, then the temporal covariance matrix of the nth receive channel can be obtained as

$$\boldsymbol{R}_{t;l;n} = \text{E}\left(\boldsymbol{X}_l((n-1)K+1:nK)\,\boldsymbol{X}_l^{\text{H}}((n-1)K+1:nK)\right) \qquad (19)$$

It is noteworthy that, according to RMB criterion [20], the estimation of clutter covariance matrix requires more than twice the number of samples to ensure that the signal to clutter plus noise ratio (SCNR) loss is less than 3dB. Hence, when estimating the temporal covariance matrix using the data of elements, it is also necessary that the number of element is twice as large as the number of pulse. In practical scenarios, the condition that the number of elements of airborne phased array radar is more than twice the number of pulses is not always satisfied, so it is necessary to achieve this requirement by Doppler filter bank [21], [22] or partial pulse selection. The Doppler filter bank or partial pulse selection can be completed by means of the dimension reduction matrix $\boldsymbol{T}_a$ [10]. Meanwhile, in order to guarantee the reversibility of the clutter temporal covariance matrix, the diagonal loading technique [23] must be used. Therefore, the temporal covariance matrix of the lth range cell can be estimated as

$$\begin{aligned}
\boldsymbol{R}_{t;l} &= \frac{1}{N}\sum_{n=1}^{N}\boldsymbol{T}_a^{\text{H}}\boldsymbol{R}_{t;l;n}\boldsymbol{T}_a + \delta^2\boldsymbol{I} \\
&= \frac{1}{N}\sum_{n=1}^{N}\boldsymbol{T}_a^{\text{H}}\boldsymbol{X}_l((n-1)K+1:nK) \\
&\quad \cdot \boldsymbol{X}_l((n-1)K+1:nK)^{\text{H}}\boldsymbol{T}_a + \delta^2\boldsymbol{I}
\end{aligned} \qquad (20)$$

where δ^2 denotes the loading coefficient.

In order to accurately reflect the distinction between two temporal clutter covariance matrices, we introduce Riemann distance. The Riemann distances of reversible matrices $\boldsymbol{A}$ and $\boldsymbol{B}$ can be defined as [24]

$$d_R(\boldsymbol{A},\boldsymbol{B}) = \left\|\log\left(\boldsymbol{A}^{-1}\boldsymbol{B}\right)\right\|_{\text{F}} = \left(\sum_{i=1}^{\bar{N}}\log^2(\lambda_i)\right)^{\frac{1}{2}} \qquad (21)$$

where λ_i denotes the eigenvalue of $\boldsymbol{A}^{-1}\boldsymbol{B}$, $\bar{N}$ denotes the dimension of $\boldsymbol{A}$ or $\boldsymbol{B}$. The Riemann distance $d_R(\boldsymbol{A},\boldsymbol{B})$ reflects the degree of $\boldsymbol{A}$ whitening $\boldsymbol{B}$. If $\boldsymbol{A}$ and $\boldsymbol{B}$ are both constructed from independent and identically distributed clutter data, then $\boldsymbol{A}^{-1}\boldsymbol{B} \approx \boldsymbol{I}$, and then $d_R(\boldsymbol{A},\boldsymbol{B}) \approx 0$ can be obtained.

However, the Riemann distance define does not satisfy the symmetry of mathematical distance, i.e.,

$$d_R(\boldsymbol{A},\boldsymbol{B}) \neq d_R(\boldsymbol{B},\boldsymbol{A}) \qquad (22)$$

If the covariance matrices $\boldsymbol{A}$ and $\boldsymbol{B}$ have the same structure, but the power of clutter constituting the matrix $\boldsymbol{A}$ is higher than that of $\boldsymbol{B}$, then the distance will not increase, because the clutter in $\boldsymbol{B}$ is over whitened by $\boldsymbol{A}$. Conversely, the distance increases. This will be a problem in measuring the difference between two clutter covariance matrices. Hence, we can solve this problem by defining a symmetric Riemann distance:

$$\bar{d}_R(\boldsymbol{A},\boldsymbol{B}) = \left(\frac{\left[d_R^2(\boldsymbol{A},\boldsymbol{B}) + d_R^2(\boldsymbol{B},\boldsymbol{A})\right]}{2}\right)^{\frac{1}{2}} \qquad (23)$$

Because the clutter range nonstationarity is a continuous gradual process which is reflected on multiple range cells, it is not accurate to measure the clutter nonstationarity by the Riemann distance of temporal clutter covariance matrices in only two range cells. To solve this problem, we propose the concept of the Riemann mean distance of L_p temporal clutter covariance matrices, which is defined as

$$\text{DR} = \frac{1}{L_p}\sum_{l=1}^{L_p}\bar{d}_R\left(\boldsymbol{R}_{t;l},\bar{\boldsymbol{R}}\right) \qquad (24)$$

where $\bar{\boldsymbol{R}} = \frac{1}{L_p}\sum_{l=1}^{L_p}\boldsymbol{R}_{t;l}$. Therefore, for the clutter range stationarity of continuous multiple range cells, the degree of nonstationarity can be measured by the value of (24), which realizes the quantitative measurement of the clutter range nonstationarity. This also provides a way to realize the adaptive division of the nonstationary clutter region in Fig. 5.

Assuming that there are L range cells in the clutter range-Doppler spectrum, we select L_p range cells from the farthest, i.e., the temporal covariance matrices of the $L - L_p + 1$th to the Lth range cells, and calculate their Riemann mean distance DR_{L-L_p+1} with (24), and then compare the result with the threshold value DR_m. If less than the threshold value, we continue to select the temporal covariance matrices of the $L-L_p$th to the $L-1$th range cells. Repeat the above steps until

a certain Riemann mean distance occurs to make $\mathrm{DR}_{L_\mathrm{f}} \geq \mathrm{DR}_\mathrm{m}$. At this time, the L_fth range cell is considered as the nonstationary clutter region dividing line 2 in Fig. 5. For easy of understanding, we summarize this algorithm in Table 2.

TABLE 2. The algorithm for determining dividing line 2.

Set the key parameters: DR_m, T_a, L_p
Calculate the total number of range cell: $L=c/(2f_r\Delta R)$, where c denotes the light velocity

---

Estimate the clutter temporal covariance matrix $R_\mathrm{t}\{l\}$, $l = 1, 2, 3, \ldots\ldots, L$
  for $l = 1 : L$

$$R_\mathrm{t}\{l\} = \frac{1}{N}\sum_{n=1}^{N} T_a^\mathrm{H} X_l\big((n-1)K+1:nK\big)$$

$$\mathrm{g}X_l\big((n-1)K+1:nK\big)^\mathrm{H} T_a + \sigma^2 I$$

  end

Determine the L_fth range cell where the diving line 2 locates
  $j = -1$
  Repeat:
    1. $j = j + 1$

$$2.\ \ \bar{R} = \frac{1}{L_\mathrm{p}}\sum_{l=1}^{L_\mathrm{p}} R_\mathrm{t}\{L - L_\mathrm{p} + l - j\}$$

$$3.\ \ \mathrm{DR}_{L-L_\mathrm{p}+1-j} = \frac{1}{L_\mathrm{p}}\sum_{l=1}^{L_\mathrm{p}} \bar{d}_\mathrm{R}\big(R_\mathrm{t}\{L - L_\mathrm{p} + l - j\}, \bar{R}\big)$$

    Until: $\mathrm{DR}_{L-L_\mathrm{p}+1-j} \geq \mathrm{DR}_\mathrm{m}$

  $L_f = L - L_\mathrm{p} + 1 + j$

Fig. 6 shows the curve of Riemann mean distance varying with range cells with $L_\mathrm{p} = 50$. If the threshold value is set as $\mathrm{DR}_\mathrm{m} = 1.25$, the 348th range cell can be identified as the nonstationary clutter region dividing line 2 in Fig. 5.
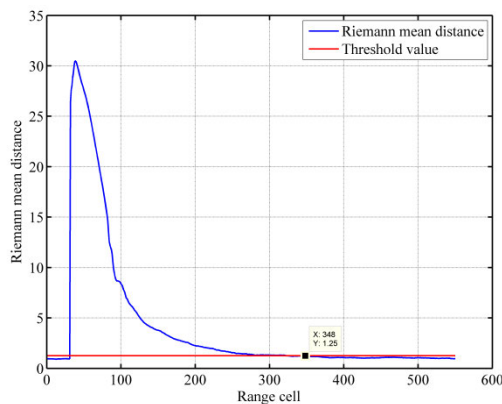

FIGURE 6. Curve of Riemann mean distance varying with range cells.

B. ADAPTIVE SEGMENTATION OF NOISE REGION

Because EAAR has no backward reflection, its clutter power mainly distributes at both ends of the Doppler domain, and the weakest clutter power is at the middle of the Doppler cells. Assuming that there are K_d Doppler cells, we successively

select h Doppler cells at the middle of the Doppler cells of the range cell at the dividing line 2, i.e., the $K_\mathrm{d}/2 - h/2 + 1$th to $K_\mathrm{d}/2+h/2$th Doppler cells, and calculate their average power as the noise base value σ_0, and set the relative threshold value as σ_m. Then slide a Doppler cell to the right, i.e., select the $K_\mathrm{d}/2 - h/2 + 2$th to $K_\mathrm{d}/2 + h/2 + 1$th Doppler cells and calculate their average power $\sigma_{K_\mathrm{d}/2+1}$, and compare it with the threshold value $\sigma_0+\sigma_\mathrm{m}$. If it is less than the value $\sigma_0+\sigma_\mathrm{m}$, repeat the above steps until $\sigma_{Kr} \geq \sigma_0 + \sigma_\mathrm{m}$ appears. At this time, the K_rth Doppler cell is considered as the pure noise region dividing line 3 in Fig. 5. For easy of understanding, we summarize this algorithm in Table 3, where S_s is the spatial steering vector in the direction of target, $S_{\mathrm{t};k}$ is the temporal steering vector in the Doppler center frequency of the kth Doppler cell. Similarly, the K_1th Doppler cell as the pure noise region dividing line 4 in Fig. 5 can be obtained by utilizing the above algorithm to the left.

TABLE 3. The algorithm for determining dividing line 3.

Set the key parameters: σ_m, h
Calculate the total number of Doppler cell: $K_\mathrm{d} = f_r/\Delta f$, where Δf denotes the bandwidth of the Doppler filter

---

Calculate the noise base value σ_0

  Select the receive date of the L_fth range cell X_{L_f}

  Calculate the echo power value of each Doppler cell $P(k)$, $k = 1, 2, 3, \ldots\ldots, K_\mathrm{d}$
    for $k = 1 : K_\mathrm{d}$

$$W = S_{\mathrm{t};k} \otimes S_\mathrm{s}$$

$$P(k) = W^\mathrm{H} X_{L_\mathrm{f}}$$

    end

$$\sigma_0 = \frac{1}{h}\sum_{k=K_\mathrm{d}/2-h/2+1}^{K_\mathrm{d}/2+h/2} P(k)$$

Determine the K_rth Doppler cell where the diving line 3 locates
  $j = 0$
  Repeat:
    1. $j = j + 1$

$$2.\ \ \sigma_{K_\mathrm{d}/2+j} = \frac{1}{h}\sum_{k=K_\mathrm{d}/2-h/2+j+1}^{K_\mathrm{d}/2+h/2+j} P(k)$$

    Until: $\sigma_{K_\mathrm{d}/2+j} \geq \sigma_0 + \sigma_\mathrm{m}$

  $K_\mathrm{r} = K_\mathrm{d}/2 + j$

Fig. 7 gives the curve of the average clutter power of the range cell in dividing line 2 varying with Doppler cells with $h = 20$ and the relative threshold $\sigma_\mathrm{m} = 6\mathrm{dB}$. According to the curve, the 145th Doppler cell and the 30th Doppler cell can be identified as the pure noise region dividing line 3 and 4 in Fig. 5.

C. METHOD PROCEDURES

In summary, the procedures of clutter suppression method based on adaptive segmentation for EAAR can be summarized as follows:
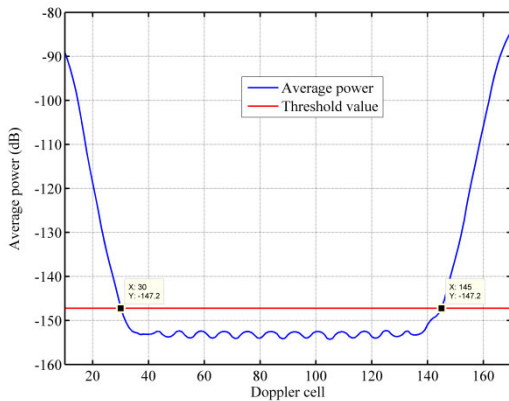
FIGURE 7. Curve of the average clutter power of the range cell in dividing line 2 varying with Doppler cells.

TABLE 4. Comparison of output SCNR (dB).

	PD processing	2D-STAP	3D-STAP	Proposed method
Target 1	15.8	20.7	24.6	24.3
Target 2	-62.3	-28.9	24.5	24.1
Target 3	-34.2	21.8	24.2	22.3
Target 4	20.6	23.2	25.3	20.8

It should be pointed out that the selection of the two thresholds DR_m and σ_m determines the performance and computational complexity of the method. If the thresholds are too high, the proportion of the nonstationary clutter region and the stationary clutter region that the method automatically divides will be reduced, which will inevitably reduce the computational complexity of the method, but the performance will also degrade as a cost. On the contrary, if the threshold values are too low, the proportion of the nonstationary clutter region and the stationary clutter region will increase, which will undoubtedly improve the clutter suppression performance, but it will also increase the computation load. Therefore, in the practical engineering application, the threshold values should be set reasonably according to the actual situation.

IV. NUMERICAL SIMULATIONS AND PERFORMANCE ANALYSIS

In this section, the clutter suppression performance of the proposed method is analyzed and assessed by computer simulations. In the simulations, the end-fire array is composed of 8 rows and 16 columns, and the number of pulse is 8. In 2D STAP, the DOF of system is 8×8, whereas in 3D STAP, the DOF of system is $8 \times 4 \times 8$, that means four receive elements are synthesized with column-subarrays, so four elevation DOFs are added. According to RMB criterion [20], for both 2D STAP and 3D STAP, the number of sample should be more than twice the DOF of system to ensure the performance loss caused by clutter covariance matrix estimation is less than 3dB. That means a large sample demands which will be difficult to be satisfied. In order to reduce the sample demands, both conventional 2D STAP method and 3D STAP method adopt element-Doppler dimension reduction technique [10], [11]. It is noteworthy that PD processing does not need samples because it does not require clutter covariance matrix estimation. Moreover, the Riemann mean distance threshold value $DR_m = 1.25$, and the clutter power relative threshold value $\sigma_m = 6dB$. Other simulation parameters are listed in Table 1.

A. COMPARISON OF SCNR LOSS

Fig. 8 shows the SCNR loss of PD processing, 2D STAP, 3D STAP, and the proposed method, respectively. We can see from Fig. 8 that PD processing works well in the pure noise region, but there is a large SCNR loss in clutter region. 2D STAP can effectively suppress the long-range stationary sidelobe clutter, but the SCNR loss is not ideal in the
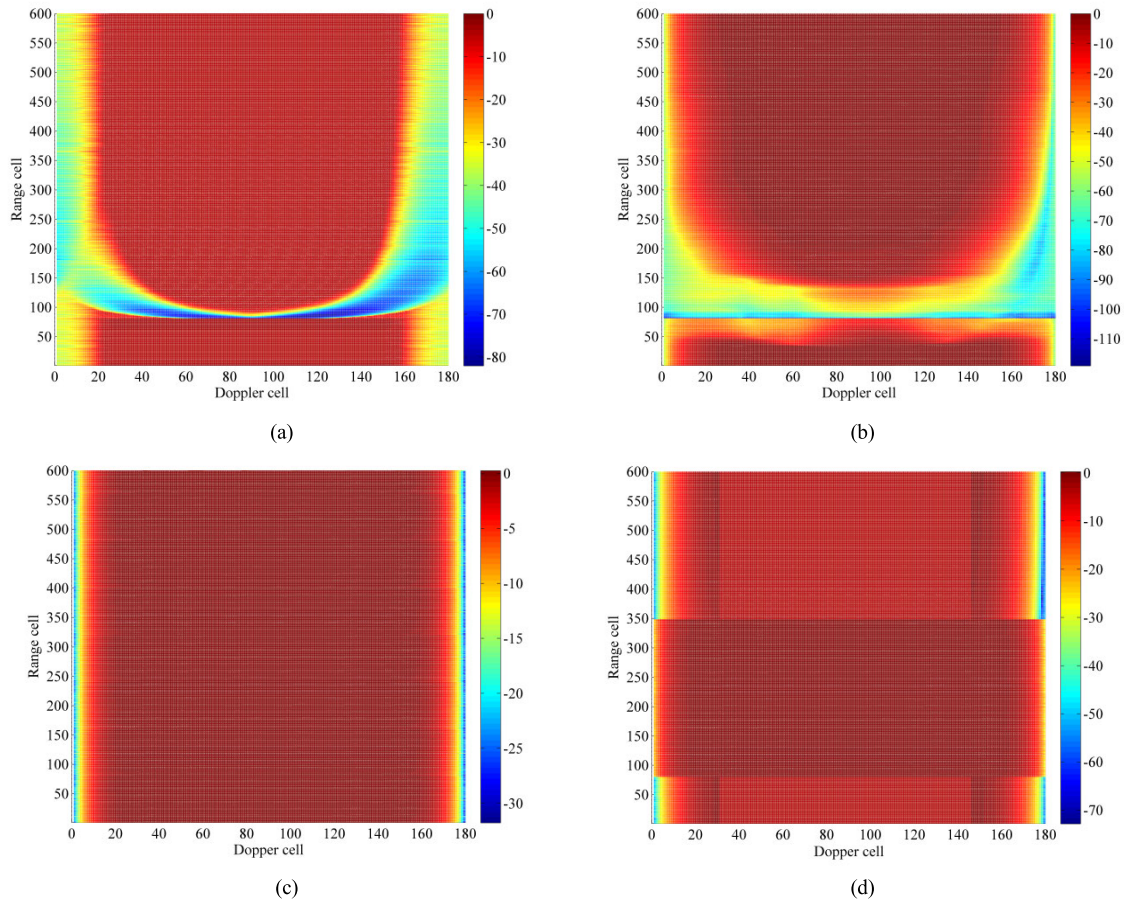
Step 1: Designing dimension reduction matrix T_a to reduce the dimension of the data of each range cell, so that the number of element is more than twice the number of pulse when estimating the temporal covariance matrix.

Step 2: Estimate the temporal covariance matrix $R_{t;l}$ of each range cell by (20).

Step 3: Calculate the Riemann mean distance DR_{L-L_p+1} of the temporal covariance matrix from $L-L_p+1$th to Lth range cells, and compare it with the threshold value DR_m. If it is less than the threshold value, continue smoothing a range cell and calculating the Riemann mean distance of the temporal covariance matrix of the selected L_p range cells until a certain Riemann mean distance appears to make $DR_{L_f} \geq DR_m$. Then, the L_fth range cell is considered as the upper dividing line of the nonstationary clutter region.

Step 4: Calculate the range cell number L_l of the altitude-line clutter, and consider that the L_lth range cell is the lower dividing line of the nonstationary clutter region.

Step 5: Process the echo data at the L_fth range cell by PD processing, and select the Doppler cells from $K_d/2-h/2+1$th to $K_d/2+h/2$th at the L_fth range cell, and then calculate their average power as the noise base value σ_0.

Step 6: Set the relative threshold value as σ_m, take the Doppler cells from $K_d/2-h/2+2$th to $K_d/2+h/2+1$th to calculate their average power value $\sigma_{K_d/2+1}$, and compare it with the threshold value $\sigma_0+\sigma_m$. If $\sigma_{K_d/2+1}$ less than $\sigma_0+\sigma_m$, continue to smooth a Doppler cell to the right and calculate the average power of the selected h Doppler cells until a certain average power appears to make $\sigma_{Kr} \geq \sigma_0+\sigma_m$. At this time, the K_rth Doppler cell is considered as the right dividing line of the pure noise region.

Step 7: Similarly, smoothing to the left using the method of step 6, we can obtain the left dividing line of the pure noise region.

Step 8: Process the nonstationary clutter region with 3D-STAP, the stationary clutter region with 2D-STAP, and the pure noise region with PD processing. At this time, the clutter suppression of radar echo is completed.

FIGURE 8. SCNR loss maps. (a) PD processing. (b) 2D STAP. (c) 3D STAP. (d) The proposed method.

TABLE 5. Computational complexity analysis.

Methods	DFT	Adaptive segmentation	Covariance matrix estimation	Weight application
PD processing	$L\dfrac{NK}{4}\log_2 N \log_2 K$	/	/	$LK_d NK$
2D-STAP	$L\dfrac{NK}{4}\log_2 N \log_2 K$	/	$LK_d(NK)^2$ $\cdot(1+NK)$	$LK_d(2(NK)^3 + 2(NK)^2 + NK)$
3D-STAP	$L\dfrac{MNK}{8}\log_2 M \log_2 N \log_2 K$	/	$LK_d(MNK)^2$ $\cdot(1+MNK)$	$LK_d(2(MNK)^3 + 2(MNK)^2 + MNK)$
Proposed method	$L_s\dfrac{NK}{4}\log_2 N \log_2 K$ $+L_n\dfrac{MNK}{8}\log_2 M \log_2 N \log_2 K$	$L_s(K^2 + 6K^3)$	$L_s K_n(NK)^2(1+NK)$ $+L_n K_d(MNK)^2$ $\cdot(1+MNK)$	$L_s K_n(2(NK)^3 + 2(NK)^2 + NK)$ $+L_n K_d(2(MNK)^3 + 2(MNK)^2 + MNK)$

short-range nonstationary clutter region. Whereas 3D STAP method has ideal SCNR loss on both short-range nonstationary and long-range stationary clutter region, and even has smaller SCNR loss in the mainlobe clutter region compared with other methods. In the proposed method, clutter can be also effectively filtered in the whole range-Doppler domain except the mainlobe clutter region by applying different clutter suppression methods to different clutter regions.

B. COMPARISON OF OUTPUT CLUTTER RESIDUE

In order to compare the clutter suppression effect of each method more clearly, we simulated several target data in the raw echo data. The location of each target is: target 1 (32, 200), target 2 (148, 120), target 3 (168, 500), target 4 (50, 400), where the abscissa is the number of Doppler cell and the ordinate is the number of range cell. Fig. 9 shows the output clutter residue of PD processing, 2D STAP, 3D STAP,
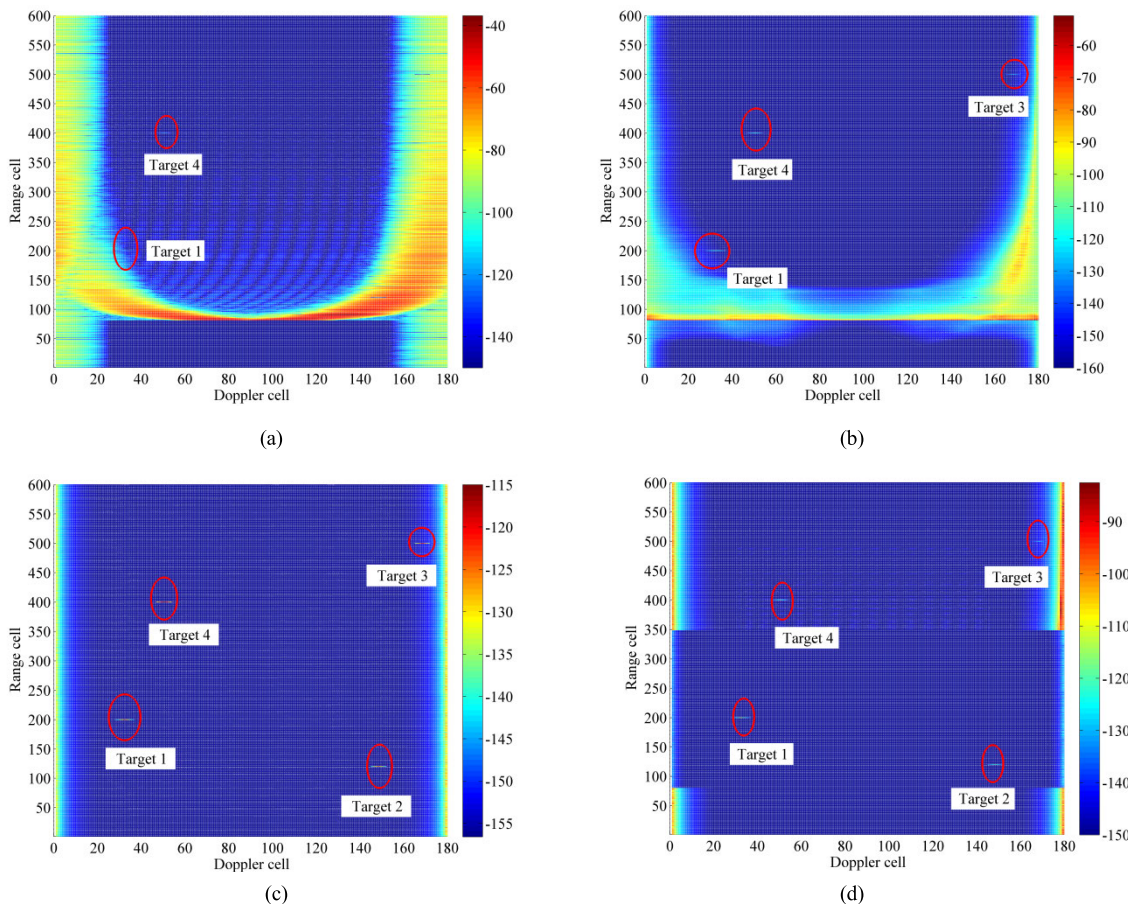
FIGURE 9. Output clutter power residue maps. (a) PD processing. (b) 2D STAP. (c) 3D STAP. (d) The proposed method.

and the proposed method, respectively. As can be seen from Fig. 9, only targets 1 and 4 in the pure noise region can be detected effectively via PD processing. Target 3 in the stationary sidelobe clutter region can also be detected via 2D STAP, but target 2 in the nonstationary clutter region is still completely submerged by clutter. The proposed method and 3D STAP can complete all targets detection.

In order to quantitatively assess the clutter suppression performance of each method and reflect the advantages of the proposed method, Fig. 10 gives the output power residue of the Doppler channel where target 2 is located. It can be seen from Fig. 10 that target 2 is still submerged by clutter via PD and 2D-STAP processing, but SCNR can reach more than 20 dB via 3D-STAP and the proposed method. Table 4 gives SCNR of each target via various methods. From the data in Table 4, we can obtain that SCNR of the four targets can reach more than 20 dB via the proposed method, i.e., all of them can be effectively detected. Compared with 3D-STAP, the proposed method only loses an average of 1 to 2 dB, which verifies the effectiveness of the proposed method.

C. COMPARISON OF COMPUTATIONAL COMPLEXITY
Assume that L range cells totally need to be processed, including L_n in the nonstationary clutter region and L_s in the stationary region, K_d Doppler cells totally need to be
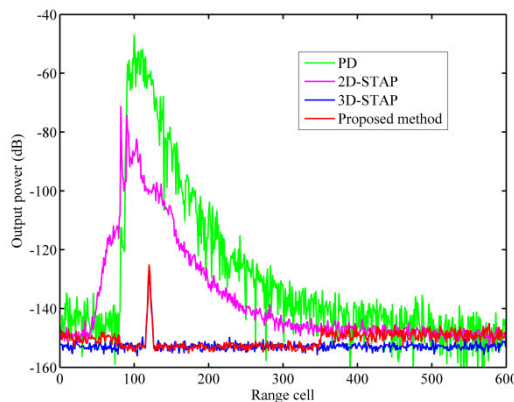

FIGURE 10. Comparison of output power.

processed, including K_n in the clutter region and K_s in the pure noise region. Then the computational complexity of the four methods for all range cells is shown in Table 5. For easy to compare intuitively, the computation load of the four methods in the case of specific parameters is given below. Under the simulation parameters in this section, the computational complexity of PD processing, 2D STAP, 3D STAP, and the proposed method are 7.03×10^6, 8.63×10^{10}, 5.46×10^{12}

and 2.74×10^{12}, respectively. Therefore, the computational complexity of 3D STAP is higher than that of other methods, whereas the computation load of the proposed method is only half of 3D STAP.

V. CONCLUSION

In this paper, we firstly analyze the clutter spectrum characteristics of EAAR systematically and draw a series of beneficial conclusions. Then, we propose a clutter suppression method based on adaptive segmentation for EAAR. In the proposed method, the concept of Riemann mean distance of temporal covariance matrix is introduced to quantify the clutter nonstationarity, and in this way we realize the adaptive segmentation of the clutter range-Doppler spectrum. The theoretical analysis and simulation results show that compared with 3D STAP, the proposed method reduces the computational complexity and sample demands in the premise of little performance loss. Compared with conventional 2D STAP, the proposed method significantly improves the clutter suppression performance in the nonstationary clutter region and ensure the effective detection of targets, which has significant engineering practical value.

REFERENCES

[1] M. Rasekh and S. Seydnejad, "Design of an adaptive wideband beamforming algorithm for conformal arrays," *IEEE Commun. Lett.*, vol. 18, no. 11, pp. 1955–1958, Nov. 2014.

[2] P. Alinezhad, S. R. Seydnejad, and D. A. Moghadam, "DOA estimation in conformal arrays based on the nested array principles," *Digit. Signal Process.*, vol. 50, pp. 191–202, Mar. 2016.

[3] R. Zhou, J. Sun, S. Wei, and J. Wang, "Synthesis of conformal array antenna for hypersonic platform SAR using modified particle swarm optimisation," *IET Radar, Sonar Navigat.*, vol. 11, no. 8, pp. 1235–1242, Apr. 2017.

[4] C. Li, X. W. Shi, H. H. Wang, and X. Li, "A compact missile-borne conformal array antenna with off-axis radiation," *Microw. Opt. Technol. Lett.*, vol. 60, no. 4, pp. 1010–1013, Apr. 2018.

[5] A. Dadgarpour, B. Zarghooni, B. S. Virdee, and T. A. Denidni, "Millimeter-wave high-gain SIW end-fire bow-tie antenna," *IEEE Trans. Antennas Propag.*, vol. 63, no. 5, pp. 2337–2342, May 2015.

[6] H. Rentang, S. Lihua, Q. Shi, and Z. Yinghui, "A novel low-profile antenna with end-fire radiation," in *Proc. CEEM*, Hangzhou, China, Nov. 2015, pp. 47–49.

[7] A. Debard, A. Clemente, C. Delaveaud, C. Djoma, P. Potier, and P. Pouliguen, "Analysis of superdirective huygens source based end-fire arrays," in *Proc. EUCAP*, Paris, France, Mar. 2017, pp. 2983–2987.

[8] A. Eshaghi, M. Tazlauanu, and M. Supinski, "Wideband end-fire phased array for WiGig applications," in *Proc. IEEE Int. Symp. Antennas Propag. USNC/URSI Nat. Radio Sci. Meeting*, San Diego, CA, USA, Jul. 2017, pp. 2559–2560.

[9] P. Wang and Z. Shen, "End-fire surface wave antenna with metasurface coating," *IEEE Access*, vol. 6, pp. 23778–23785, Apr. 2018.

[10] J. Ward, "Space-time adaptive processing for airborne radar," MIT Lincoln Lab., Lexington, MA, USA, Tech. Rep. 1015, Dec. 1994.

[11] W. L. Melvin, "A STAP overview," *IEEE Aerosp. Electron. Syst. Mag.*, vol. 19, no. 1, pp. 19–35, Jan. 2004.

[12] H. Yuan, H. Xu, K. Duan, W. Xie, W. Liu, and Y. Wang, "Sparse Bayesian learning-based space-time adaptive processing with off-grid self-calibration for airborne radar," *IEEE Access*, vol. 6, pp. 47296–47307, 2018.

[13] T. Hale, M. Temple, and M. Wicks, "Target detection in heterogeneous airborne radar interference using 3D STAP," in *Proc. IEEE Radar Conf.*, Huntsville, AL, USA, May 2003, pp. 252–257.

[14] P. M. Corbell, J. J. Perez, and M. Rangaswamy, "Enhancing GMTI performance in non-stationary clutter using 3D STAP," in *Proc. IEEE Radar Conf.*, Boston, MA, USA, Apr. 2007, pp. 647–652.

[15] C. Wen, T. Wang, and J.-X. Wu, "Range-dependent clutter suppression approach for non-side-looking airborne radar based on orthogonal waveforms," *IET Radar, Sonar Navigat.*, vol. 9, no. 2, pp. 210–220, 2015.

[16] Z. Wang, W. Xie, K. Duan, F. Gao, and Y. Wang, "Short-range clutter suppression based on subspace projection preprocessing for airborne radar," in *Proc. CIE Int. Conf. Radar*, Guangzhou, China, Oct. 2016, pp. 1–4.

[17] K. Duan, H. Yuan, H. Xu, W. Liu, and Y. Wang, "Sparsity-based non-stationary clutter suppression technique for airborne radar," *IEEE Access*, vol. 6, pp. 56162–56169, 2018.

[18] J. Liu, G. Liao, and M. Li, "A clutter spectrum compensation method for non side-looking airborne radar with range ambiguity," *Acta Electron. Sinica*, vol. 39, no. 9, pp. 2060–2066, Sep. 2011.

[19] V. Varadarajan and J. L. Krolik, "Joint space-time interpolation for distorted linear and bistatic array geometries," *IEEE Trans. Signal Process.*, vol. 54, no. 3, pp. 848–860, Mar. 2006.

[20] L. E. Brennan and L. S. Reed, "Theory of adaptive radar," *IEEE Trans. Aerosp. Electron. Syst.*, vol. AES-9, no. 2, pp. 237–252, Mar. 1973.

[21] T. Shan, Y. Ma, R. Tao, and S. Liu, "Multi-channel NLMS-based sea clutter cancellation in passive bistatic radar," *IEICE Electron. Express*, vol. 11, no. 20, pp. 1–12, Oct. 2014.

[22] S. Liu, Y. Ma, and Y. Huang, "Sea clutter cancellation for passive radar sensor exploiting multi-channel adaptive filters," *IEEE Sensors J.*, vol. 19, no. 3, pp. 982–995, Feb. 2019.

[23] Y. Ke, C. Zheng, R. Peng, and X. Li, "Robust adaptive beamforming using noise reduction preprocessing-based fully automatic diagonal loading and steering vector estimation," *IEEE Access*, vol. 5, pp. 12974–12987, Jul. 2017.

[24] C. Silva, R. Duarte, R. Goulart, and A. Trofino, "Towards a LMI approach to feature extraction improvements and classification by Riemann distance," in *Proc. ICCA*, Kathmandu, Nepal, Jun. 2016, pp. 990–995.

YONGWEI LI was born in Hengyang, Hunan, China, in 1994. He received the B.S. degree from Wuhan Early Warning Academy, Wuhan, China, in 2017, where he is currently pursuing the M.S. degree.

His current research interests include space time adaptive processing and radar signal processing.

WENCHONG XIE was born in Laiwu, Shanxi, China, in 1978. He received the B.S. and M.S. degrees from Wuhan Radar Academy, Wuhan, China, in 2000 and 2003, respectively, and the Ph.D. degree from the National University of Defense Technology, Changsha, China, in 2006.

He is currently an Associate Professor with the Key Laboratory of Radar Application Engineering, Wuhan Early Warning Academy. He has authored more than 100 articles. He holds 25 patents. He has been granted one software copyright. He is a member of the Young Scientists Club of CIE. His research interests include space time adaptive processing, radar signal processing, and adaptive signal processing. He was a recipient of the Honor of Outstanding Science and Technology Worker of Wuhan.

HUIHUANG MAO was born in Changde, Hunan, China, in 1994. He received the B.S. and M.S degrees from Wuhan Early Warning Academy, Wuhan, China, in 2016 and 2019, respectively.

He is currently an Assistant with the Department of Radar Technique, Wuhan Early Warning Academy. His current research interests include sea clutter modeling, target detection, and adaptive signal processing.

RUIJIE DONG was born in Xinjiang, China, in 1995. He received the B.S. degree from the Department of Information Countermeasure, Wuhan Early Warning Academy, Wuhan, China, in 2017, where he is currently pursuing the M.S. degree.

His current research interests include space time adaptive processing and signal intelligent processing.

● ● ●